

Composition of the Innermost Supernova Ejecta

C. Fröhlich¹, P. Hauser¹, M. Liebendörfer², G. Martínez-Pinedo³, F.-K. Thielemann¹, E. Bravo⁴, N. T. Zinner⁵, W.R. Hix⁶, K. Langanke⁵, A. Mezzacappa⁶, K. Nomoto⁷

ABSTRACT

With presently known input physics and computer simulations in 1D and 2D a self-consistent treatment of core collapse supernovae does not yet lead to successful explosions. However, there are strong indications that the delayed neutrino mechanism works combined with a multi-D convection treatment for unstable layers (possibly with the aid of rotation, magnetic fields and/or still existent uncertainties in neutrino opacities). On the other hand there is a need to provide correct nucleosynthesis yields for the progressing field of galactic evolution and observations of low metallicity stars. The innermost ejecta will be directly affected by the explosion mechanism, i.e. most strongly the yields of Fe-group nuclei for which an induced piston or thermal bomb treatment will not provide the correct yields because the effect of neutrino interactions is not included. In 1D one can mimic uncertainties in neutrino opacities, proto-neutron star core convection (leading to higher neutrino luminosities), and convection in the “gain region“ where the neutrino energy is deposited (leading to higher efficiencies in energy deposition) by variations in neutrino scattering cross sections and/or neutrino capture cross sections on nucleons. We find that both measures lead to similar results, causing explosions and a $Y_e > 0.5$ in the innermost ejected layers, due to the combined effect of a short weak interaction time scale and a negligible electron degeneracy unveiling the proton-neutron mass difference. We include all weak interactions (electron and positron capture, beta-decay, neutrino

¹Departement für Physik und Astronomie, Universität Basel, CH-4056 Basel, Switzerland

²Canadian Institute for Theoretical Astrophysics, University of Toronto, Toronto ON M5S 3H8, Canada

³ICREA and Institut d’Estudis Espacials de Catalunya, Universitat Autònoma de Barcelona, E-08193 Barcelona, Spain

⁴Universitat Politècnica de Catalunya, E-08034 Barcelona, Spain

⁵Institute of Physics and Astronomy, Aarhus University, Aarhus C, Denmark

⁶Physics Division, Oak Ridge National Laboratory, Oak Ridge TN 37831-6374, USA

⁷Department of Astronomy, University of Tokyo, Tokyo 113-033, Japan

and anti-neutrino capture on nuclei, and neutrino and antineutrino capture on nucleons) and present first nucleosynthesis results for these innermost ejected layers to discuss how they improve predictions for Fe-group nuclei. The proton-rich environment results in enhanced abundances of ^{45}Sc , ^{49}Ti , and ^{64}Zn as requested by chemical evolution studies and observations of low metallicity stars.

Subject headings: supernovae, nucleosynthesis

1. Introduction

The problem of core collapse supernova explosions is an old one and the attempt to understand the mechanism has been ongoing for more than 30 years. The idea that a massive star proceeds through all burning stages from H to Si-burning, finally leading to the collapse of the resulting Fe-core to nuclear densities by the formation of a neutron star has long been discussed (e.g. Baade & Zwicky 1934; Oppenheimer & Snyder 1939; Arnett & Schramm 1973). Since the sixties the explosion mechanism has been related to neutrino emission from the hot collapsed core (e.g. Colgate & White 1966; Bethe & Wilson 1985; Bethe 1990) interrupted by a period when it was speculated that the strength of the bounce at nuclear densities could permit shock waves with sufficient energies to lead to prompt explosions (e.g. Baron et al. 1985, 1987). However, this became questionable when previously neglected neutrino scattering processes were introduced (e.g. neutrino-electron scattering), which permitted to replace lost low energy neutrinos, leading to a continuous energy leakage and to the death of the prompt shock within 10 ms after bounce (Bruenn 1989; Myra & Bludman 1989).

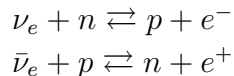
Since then, and with the first neutrino detection from a core collapse supernova (SN1987A, see e.g. Koshiha (1992); Burrows (1990)), the hope has been that further improvement would lead to successful explosions via energy deposition through neutrino and anti-neutrino captures on neutrons and protons ($\nu_e + n \rightarrow p + e^-$, $\bar{\nu}_e + p \rightarrow n + e^+$). Two different paths were explored. 1. Convective instabilities, but with still simplified neutrino transport, causing either (a) convective transport in the core and leading to higher neutrino luminosities (e.g. Keil et al. 1996) or (b) higher energy deposition efficiencies in convective regions (Mayle & Wilson 1988; Janka & Müller 1996; Herant et al. 1994; Fryer & Warren 2004). 2. Improved neutrino transport schemes, leading to higher neutrino luminosities via the full solution of the Boltzmann transport equation for neutrino scattering and neutrino reactions (Mezzacappa & Bruenn 1993a,b; Messer et al. 1998).

However, the recent years have shown that with the present knowledge of physical

processes a supernova explosion cannot be explained in 1D spherically symmetric nor 2D rotationally symmetric radiation-hydro calculations (Rampp & Janka 2000; Mezzacappa et al. 2001; Liebendörfer et al. 2001; Liebendörfer et al. 2001; Buras et al. 2003; Janka et al. 2003; Hix et al. 2003; Langanke et al. 2003; Thompson et al. 2003). This leaves us with two dilemmata. First of all, the fundamental one that the supernova mechanism is still not understood. Second, there seems no way to predict the correct supernova nucleosynthesis yields. This is a problem for itself, but also for the strongly expanding field of galactic chemical evolution calculations, being energized by the large amount of upcoming abundance observations from low metallicity stars (e.g. Argast et al. 2002, 2004; Sneden et al. 2003; Cayrel et al. 2004; Honda et al. 2004).

Supernova nucleosynthesis predictions have a long tradition (Woosley & Weaver 1986; Thielemann et al. 1990; Woosley & Weaver 1995; Thielemann et al. 1996; Nomoto et al. 1997; Nakamura et al. 2001; Rauscher et al. 2002; Chieffi & Limongi 2002; Umeda & Nomoto 2005). But all of these predictions relied on an artificially introduced explosion, either via a piston or a thermal bomb (Aufderheide et al. 1991) introduced into the progenitor star model. In this approach, the mass cut between the ejecta and the remnant does not emerge from the simulation, but it has to be determined from additional conditions. While approach of artificially introduced explosions makes sense and is fully correct for the outer stellar layers, provided we know the correct explosion energy to be dumped into the shock front (on the order of 10^{51} erg seen in observations), it clearly is incorrect for the innermost ejected layers which should be directly related to the physical processes causing the explosion. This affects the Fe-group composition, discussed in detail in Thielemann et al. (1996), which was also recognized as a clear problem by Nakamura et al. (1999); Chieffi & Limongi (2002); Umeda & Nomoto (2002). The problem is also linked to the so-called neutrino wind, emitted seconds after the supernova explosion, and considered as a possible source of the r-process to produce the heaviest elements via neutron captures (Takahashi et al. 1994; Woosley et al. 1994; Qian et al. 1997; Thompson et al. 2001; Wanajo et al. 2001; Terasawa et al. 2002; Thompson et al. 2003).

The dominant quantity to describe nucleosynthesis correctly in the innermost ejecta is the $Y_e = \langle Z/A \rangle$ in the layers undergoing explosive Si-burning. This Y_e is set by the weak interactions in the explosively burning layers, i.e. electron and positron captures, beta-decays, and neutrino or antineutrino captures. The dominant reactions in hot photodisintegrated matter, consisting mainly of neutrons and protons are:



We will show in section 2 that these reactions lead to an equilibrium for Y_e on a time scale shorter than explosive burning. We will also show that the resulting Y_e in the innermost ejected layers is close to 0.5, in some areas even exceeding 0.5. This has been strongly postulated as a requirement in order not to violate abundance constraints from galactic evolution and solar abundances (Thielemann et al. 1996).

The question arises how one could simulate realistically this behavior, given the existing problems with self-consistent explosions. Discussed improvements which could lead to successful supernova explosions are rotation and magnetic fields (e.g. Thompson 2000; Thompson et al. 2004) or uncertainties in neutrino opacities (see e.g. Burrows et al. 2004) or other microphysics properties. They would introduce additional mixing at the neutrino sphere and convective transport or change the neutrino luminosity via improved opacities. This leads to the two options for successful explosion as discussed above: (a) enhanced neutrino luminosities or (b) enhanced deposition efficiencies for neutrino capture in convective layers. These effects can be simulated in two ways: (a) Boosting the neutrino luminosity via a scaling (reduction) of the neutrino scattering cross section on nucleons while keeping the electron/positron and neutrino/antineutrino capture cross sections on neutrons and protons at their original values. (b) Boosting the energy deposition efficiencies by enhancing the neutrino and anti-neutrino captures on neutrons and protons. We cannot claim that this is a self-consistent treatment, but no external energy is required to produce a successful explosion with a consistently emerging mass cut between neutron star and ejecta. Moreover, our treatment guarantees that Y_e is consistently determined by all weak interactions processes.

2. Matter in a neutrino field

Even if we do not know how significantly absorptions of the neutrinos emitted from the protoneutron star surface contribute actually to the revival of the shock, it is necessary to include the neutrinos and their copious interaction with the matter in the vicinity of the protoneutron star. If the explosion is launched such that the mass cut is directly determined by the early dynamics of the explosion, this neutrino heated material will contribute to the deepest layers of the ejecta. If the mass cut is determined later in a fallback process, contributions are only possible by strong mixing. In any case, this neutrino heated material will have significantly changed its composition with respect to its original progenitor composition. Hence, we investigate in this section the conditions in ejecta that are subject to large neutrino fluxes.

Most neutrinos receive their energy in the vicinity of the neutrinospheres at a radius of ~ 70 km. Before the launch of the explosion, about two thirds of the emitted neutrinos

stem from the infalling matter which is squeezed in the gravitational potential and settles on the surface of the protoneutron star. After the launch of the explosion, this contribution will decrease with the accretion rate and the less accretion-sensitive neutrino diffusion flux from the hot protoneutron star will dominate. A more detailed description of this transition, however, requires multi-dimensional simulations because the evolution of the accretion rate shows quite aspherical features with narrow downflows and broad upflows (Herant et al. 1994; Burrows et al. 1995; Janka & Müller 1996; Buras et al. 2003) that are ignored in spherical symmetry. The emitted electron flavor neutrinos may essentially interact with the material behind the accretion shock out to radii of about 300 km (“essential” meaning electron fraction changes on a time scale of 100 ms). The interactions decrease steeply with increasing radius as the neutrino density is inverse proportional to the surface area of the enclosed sphere ($1/r^2$ dependence). In order to illustrate the basic behaviour of shock-heated matter in a neutrino bath, we first consider only the four dominant reactions, electron capture on free protons $e^- + p \rightleftharpoons n + \nu_e$, and positron capture on free neutrons $e^+ + n \rightleftharpoons p + \bar{\nu}_e$, and their inverse reactions. Two independent conditions are required to specify the electron fraction and the entropy of the material, for example weak equilibrium and thermal balance.

The change of the electron fraction, Y_e , with time, t , is given by Eqs. (C15) and (C20) in (Bruenn 1985). The neutrino opacities, χ , and emissivities, j , are linked by the reciprocity relation described in Eqs. (C7) and (C8) in the above reference. The reciprocity relation involves the temperature, $kT = \beta^{-1}$, the neutrino energy, E , measured in the rest frame of the fluid, and the chemical potentials, μ_n , μ_p , and μ_e , for neutrons, protons, and electrons respectively. As the particle rest masses are included in these chemical potentials we use the mass difference between neutron and proton, $Q = 1.2935$ MeV, to define the quantity $\tilde{\mu} = \mu_n - \mu_p - Q$ for the kinetic part in the difference between the neutron and proton chemical potentials. We can therefore label contributions from electron, positron, neutrino, and antineutrino capture with EC , PC , NC , and AC respectively, and express the opacities in NC and AC by the neutrino emissivities. After having collected all terms that do not depend on the neutrino energy into a common factor, K , we write the total change in the electron fraction in the following form:

$$\frac{1}{c} \frac{dY_e}{dt} = K \int dE E^2 [h(E + Q)(-EC + NC) + \Theta(E - Q - m_e)h(E - Q)(PC - AC)] \quad (1)$$

Here, the details of the roughly quadratic energy dependence of the cross sections are hidden in the function

$$h(x) = x^2 \left[1 - \left(\frac{m_e c^2}{x} \right)^2 \right]^{1/2},$$

and a step function $\Theta(x)$ is used to describe the energy threshold in the positron and antineutrino capture reactions. A very similar equation can be used to describe the change of

the specific internal energy, e , of the fluid due to neutrino interactions:

$$\frac{1}{c} \frac{de}{dt} = K \int dE E^3 [h(E+Q)(-EC+NC) + \Theta(E-Q-m_e)h(E-Q)(-PC+AC)] \quad (2)$$

The contributions to Eqs. (1) and (2) from the individual reactions are given by

$$\begin{aligned} EC &= \frac{1}{1 + e^{\beta(E+Q-\mu_e)}} (1 - f_\nu) \\ NC &= \frac{e^{\beta(E+Q-\mu_e)}}{1 + e^{\beta(E+Q-\mu_e)}} e^{\beta\tilde{\mu}} f_\nu \\ PC &= \frac{1}{1 + e^{\beta(E-Q+\mu_e)}} e^{\beta\tilde{\mu}} (1 - f_{\bar{\nu}}) \\ AC &= \frac{e^{\beta(E-Q+\mu_e)}}{1 + e^{\beta(E-Q+\mu_e)}} f_{\bar{\nu}} \end{aligned} \quad (3)$$

where $f(E)$ is the neutrino distribution function in the rest frame of the fluid.

Note that Eqs. (1) and (2) do not presume that the neutrinos are in equilibrium with matter, nor that they assume any particular spectrum. Some of these assumptions, however, lead to useful analytical formulas for the equilibrium electron fraction. Dominance of the neutrino absorption terms has been assumed for the investigation of the r-process in the neutrino wind of a protoneutron star (Qian & Woosley 1996; Thompson et al. 2001); and the cases where emission terms dominate or where the neutrinos are in thermal equilibrium have been analysed in a study of gamma-ray burst fireballs (Beloborodov 2003). The balance between the four reactions in Eq. (3) is determined by two exponentials, $\exp(\beta\tilde{\mu})$ and $\exp(\beta[E \pm Q \mp \mu_e])$. The former simply reflects the difference between the neutron and proton abundances. The latter depends on a competition between the neutrino energy, E , the mass difference between neutrons and protons, Q , and the electron chemical potential, μ_e . Under idealized conditions, either one of these three quantities can dominate.

For large abundances of neutrinos at very high energies the term $\exp(\beta E)$ is large and the neutrino absorption terms, NC and AC in Eq. (3), dominate over neutrino emission. Hence, if the abundance of high energy neutrinos is large, the equilibrium Y_e is mainly determined by the balance between neutrino and antineutrino absorption as determined by the unknown neutrino distribution functions.

The electron chemical potential might dominate the exponential at smaller neutrino energies, for example when the electrons are degenerate. In this case, $\exp(\beta(E+Q-\mu_e))$ in Eq. (3) is small and $\exp(\beta(E-Q+\mu_e))$ becomes large. Hence, neutrino absorption, NC , and positron capture, PC , are suppressed and the electron fraction decreases because of more prolific electron captures and antineutrino absorptions. Balance is only established

when the proton fraction has sufficiently decreased that the factor $\exp(\beta\tilde{\mu})$ in *NC* and *PC* compensates for the suppression. But $\tilde{\mu}$ is only positive if the neutron abundance is larger than the proton abundance. An equilibrium electron fraction can only exist for $Y_e < 0.5$ as expected under electron degenerate conditions.

The electron chemical potential is small in a plasma with nondegenerate electrons and in this case the neutron to proton mass difference, Q , may actually dominate the exponentials in the balance equations, making $\exp(\beta(E + Q - \mu_e))$ in Eq. (3) larger and $\exp(\beta(E - Q + \mu_e))$ smaller. Just inverse than under degenerate conditions, *NC* and *PC* are favored and a factor $\exp(\beta\tilde{\mu}) < 1$ is assumed in equilibrium. Under these conditions, equilibrium can establish at $Y_e > 0.5$. According to the analytical investigation in Beloborodov (2003) for the *EC* and *PC* reactions, this situation will occur if the electron chemical potential fulfills the condition $\mu_e < Q/2$. The larger binding energy favors protons over neutrons. High electron fractions below $Y_e = 0.5$ have been predicted for supernova explosions (Thompson 2000). But recent supernova simulations with accurate neutrino transport have even exceeded the estimates, consistently finding values of $Y_e > 0.5$ in the vicinity of the mass cut in explosion settings (Liebendörfer et al. 2001; Buras et al. 2003; Janka et al. 2003; Thompson et al. 2004; Fröhlich et al. 2004; Pruet et al. 2004).

3. Hydrodynamical simulations

The framework for this investigation are spherically symmetric simulations with general relativistic Boltzmann neutrino transport, we refer to (Mezzacappa & Messer 1999; Liebendörfer et al. 2004) for a detailed description of the code *AGILE-BOLTZTRAN*. It features a dynamically adaptive grid (Liebendörfer et al. 2002) that zeroes grid points in to the developing mass cut. The simulations are performed until a minimum density of $\sim 10^6$ g/cm³ develops in the region of the bifurcation between the ejecta and the remnant. At this time, mass zones are becoming very small and we have to stop the run because of ill-conditioned Jacobi matrices in the Newton-Raphson scheme. The simulations are then continued by an explicit hydrodynamical code. The code employs an explicit difference scheme similar to Colgate & White (1966) and a simplified nuclear reaction network as explained in Bravo et al. (1993). The dynamical evolution of the region internal to the mass cut is substituted by a radiation bubble with a static gravitational potential corresponding to the gravitational mass enclosed by the mass cut. The bubble is assumed to expand adiabatically so that the pressure at the mass cut radius (R_c) is proportional to R_c^{-4} .

We use two different approaches to enforce explosions in otherwise non-explosive supernova models. We parametrize the neutral current neutrino scattering opacities on free

nucleons with a factor ranging from 0.1 to 0.7 and use a finite differencing¹ that helps to artificially increase the diffusive fluxes in regions of very high matter density. The net result is a faster deleptonization of the protoneutron star such that the neutrino luminosities are boosted in the heating region. For the sake of computational efficiency, this first series of parametrized runs (series A) has been calculated with the lowest possible angular resolution involving only inwards and outwards propagating neutrinos. However, all of these measures only affect the propagation of neutrinos in the model; the models are still closed and respect energy and lepton number conservation. We expect that series A represent a simplification of the phenomenology of supernovae that would be driven by higher neutrino luminosities than in the standard cases. Under discussion are for example different forms of protoneutron star convection (Wilson & Mayle 1993; Keil et al. 1996; Mezzacappa et al. 1998; Bruenn et al. 2004) or improvements in the uncertain high density input physics.

With progress in computer speed and code parallelization, we were able to perform simulations using standard resolution (6 angular bins, 12 energy groups) for the Boltzmann neutrino transport in the parameter study for series B. Series B also includes the weak magnetism corrections in the neutrino cross sections (Horowitz 2002). Explosions are enforced by multiplying the emissivities and absorptivities (i.e. the reaction rates for forward and backward reactions in $\nu_e + n \rightleftharpoons p + e^-$ and $\bar{\nu}_e + p \rightleftharpoons n + e^+$) in the heating region by equal factors. This enhances the time scale for neutrino heating without changing the important equilibrium Y_e and temperature. We hope to mimic with this approach a potentially increased heating efficiency in the heating region as it is expected in combination with overturn in this convectively unstable domain (Herant et al. 1994; Burrows et al. 1995; Janka & Müller 1996; Mezzacappa et al. 1998; Buras et al. 2003).

¹According to Eq. (91) in (Mezzacappa & Bruenn 1993a) instead of Eq. (56) in (Liebendörfer et al. 2004), see sections 3.3.2 and 4.1 in the latter reference for details.

Table 1: Name and properties of the discussed runs

Run	Parameter	E_{expl} [erg]	$m_{\text{cut}}[M_{\odot}]$	$t_{v>0}$ [s]	t_{end} [s]
A60	60% scatt.	0.24×10^{51}	1.585	0.46	0.64
A40	40% scatt.	0.78×10^{51}	1.511	0.27	0.53
A20	20% scatt.	1.24×10^{51}	1.444	0.20	0.44
B05	factor 5	0.31×10^{51}	1.586	0.38	0.53
B07	factor 7	0.78×10^{51}	1.531	0.26	0.43
B10	factor 10	1.12×10^{51}	1.509	0.24	0.40

Note. — The parameter of series A specifies the percentage of neutral current interactions considered in the model. The parameter of series B specifies the enhancement of the heating time scale. The time after bounce where we had to stop the runs with neutrino transport is displayed in the last column labelled by t_{end} . The time of the first appearance of positive velocities is given in the column $t_{v>0}$. The mass cut m_{cut} has been determined at the point where the total energy integrated from outside inwards reaches a maximum. The estimate for the explosion energy E_{expl} has been composed from the total energy of the unbound material between the masscut and the shock front at t_{end} (mostly material that was in NSE) and a correction for the total energy of the bound layers ahead of the shock at progenitor composition.

All models are based on a progenitor model with a main sequence mass of $20 M_{\odot}$ (Nomoto & Hashimoto 1988). The parameters in series A and B are chosen such that each series contributes with a barely exploding model, an extremely exploding model (in terms of parameter range, the explosion energy itself seems to saturate around 1.2×10^{51} erg), and a model with average parameter setting. Important properties of the different runs are listed in Table 1.

Figure 1a presents an overview of the shock trajectories. Runs from series A are presented with solid lines and runs from series B with dashed lines. The legend in Figure 1c also applies to Figure 1a. In all runs, the accretion front stalls at about 100 ms after bounce at a radius between 180 and 300 km depending on the parameters. The accretion front is slowly receding in the more optimistic models. Shortly before 200 ms after bounce, the accretion front moves outward again. There may still be some additional delay until the inwards drifting material behind the shock reverses its velocity and starts to accumulate kinetic energy for the ejection. This happens at 199 ms after bounce for the fastest explosion (A20) and at 461 ms after bounce for the slowest run (A60). Bruenn’s suggestion to locate the mass cut where the integrated total energy of all external material assumes a maximum agrees well with the actual bifurcation in the mass trajectories. The mass cuts, m_{cut} , range from $1.444 M_{\odot}$ to $1.585 M_{\odot}$.

4. Conditions of matter in the vicinity of the mass cut

In the following, we trace a mass element in the exemplary run A40. We choose a mass element that is $0.005 M_{\odot}$ outside of the mass cut. The trajectory of this mass element is represented in Figure 1a by a dotted line: At first, the element is falling into the gravitational potential. After 200 ms it passes through the accretion shock at about 300 km radius and is instantaneously decelerated. A second phase of drifting around in the heating region follows until about 400 ms after bounce. Finally, the mass element is ejected to larger radii.

Figure 1b illustrates important energy scales along the trajectory. The dashed and dash-dotted thick lines at the top of the graph indicate the neutrino temperature for the electron neutrinos and antineutrinos respectively. They show a rising trend in the first half of the graph. This is because the protoneutron star shrinks and the neutrinospheres become hotter as they shift deeper into the gravitational well. The discontinuity at the crossing of the shock front stems from the Doppler shift when the mass element crosses the velocity jump at the accretion front. The change of the rise into a decline around $t = 350$ ms after bounce is due to the decrease of the accretion rate after the launch of the explosion. Rising neutrino temperatures are resumed at a very small accretion rate after $t = 450$ ms.

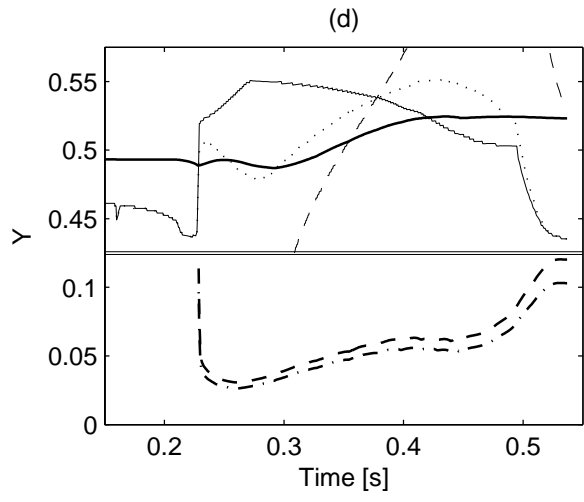
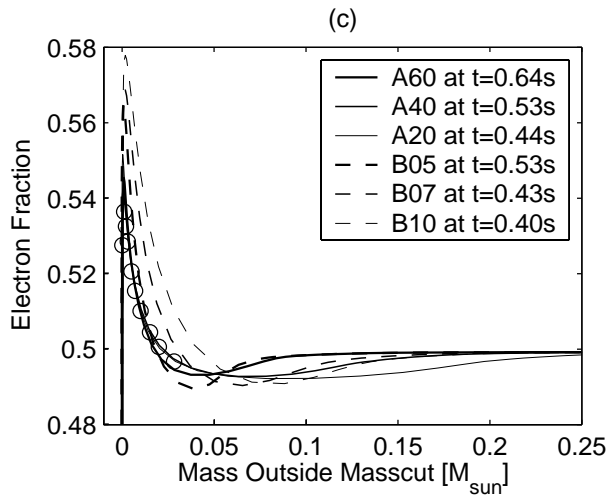
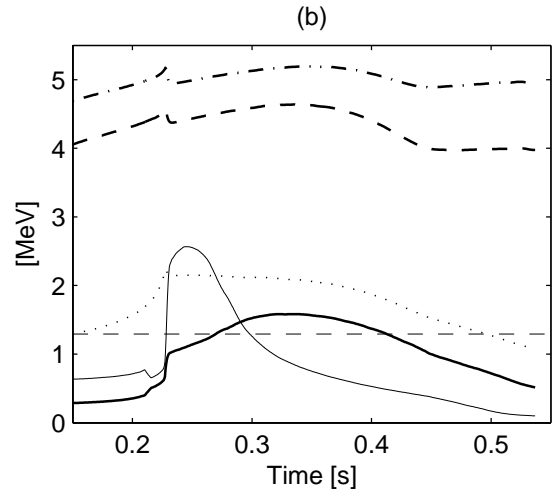
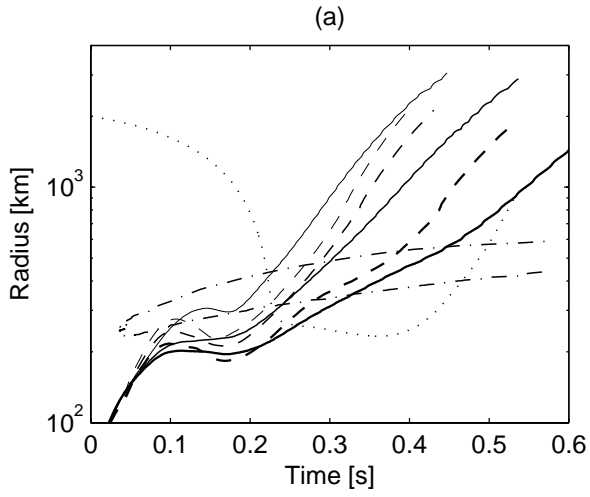


Fig. 1.— (a) Trajectories of the (accretion-)shock as a function of time. Series A (solid lines) explodes because of artificially increased core diffusion luminosities. The neutral current neutrino opacity is used as parameter with 20% of the standard values (thin line), with 40% (medium line width), and with 60% (thick line). Series B (dashed lines) explodes because of artificially accelerated neutrino absorption and emission processes in the heating region. The acceleration factors are 10 (thin line), 7 (medium line width), and 5 (thick line). See also the legend in graph (c) for an identification of the shock trajectories. The dotted line traces the trajectory of a representative fluid element located at $0.005 M_{\odot}$ outside of the estimated mass cut. Its electron fraction and specific energy can change by weak interactions on a time scale represented by the dot-dashed line (reaction time scale as a function of radius). The lower branch belongs to the infall phase and the upper branch to the ejection.

(b) Energy scales sampled at the representative fluid element as a function of time. Thick lines show the fluid temperature (solid), the neutrino temperature (dashed), and the antineutrino temperature (dot-dashed). Thin lines represent the electron chemical potential (solid), the mass difference between neutron and proton (dashed), and the temperature that would obtain after infinite exposure to the neutrino field (dotted). The electrons in the representative fluid element are degenerate during collapse and after shock compression. Neutrino heating and expansion during the ejection lifts the electron degeneracy and the neutron to proton mass difference becomes the dominant energy scale.

(d) Abundances sampled at the representative fluid element. Thick lines show the electron fraction (solid), neutrino fraction (dashed), and antineutrino fraction (dot-dashed). Thin lines represent electron fractions that would obtain after infinite exposure to the neutrino field. Only neutrino absorptions have been considered for the solid line and only emissions have been considered for the dashed line. The dotted line includes all charged current reactions. Graphs (b) and (d) show that the electron fraction is first kept high by neutrino absorptions, later by neutrino emissions. The electron fraction at freezeout is determined by competition between the neutrino interaction rates and the matter ejection timescale.

(c) Electron fraction as function of mass when the runs are stopped (0.4–0.6 s after bounce) with (A) reduction of the neutral current scattering opacities (solid lines), or (B) enhancement of the reaction timescales (dashed lines). The open circles represent the final electron fractions of run A40 after the freezeout of charged current interactions.

With the full neutrino spectrum and abundances from the simulation and the matter density as input, we calculate the equilibrium matter temperature along the trajectory according to Eq. (2) by requiring $de/dt = 0$. For consistency with the simulation, we have also included the charged current reactions with nuclei according to the simple model described in (Bruenn 1985). The dotted line in Figure 1b shows the equilibrium temperature of matter subject to the neutrino luminosities (the neutrinos themselves are not in thermal equilibrium with matter, their temperature is set in the vicinity of the neutrinospheres, where the matter temperature is higher). The lower part of Figure 1b shows the matter temperature (thick solid line) and the electron chemical potential (thin solid line). The electrons are degenerate in the cool infalling matter. The first little blip in the trajectory after $t = 200$ ms is due to the burning of the initial silicon layer to nuclear statistical equilibrium. It causes a slight rise in the temperature and decline in the electron chemical potential. The pronounced step up in both quantities is due to shock compression when the mass element hits the accretion front. During the drift in the heating region, we note a temperature increase towards temperature balance (dotted line) by neutrino heating. The onset of the explosion during this time also leads to an expansion and drop in matter density. Both effects work together to lift the electron degeneracy shortly before 300 ms after bounce (crossing of temperature and electron chemical potential lines). The evolution during the third ejection phase is characterised by a density decrease. The weak interaction rates decrease and the temperature declines due to adiabatic expansion. The electrons stay nondegenerate and the electron chemical potential remains smaller than the neutron to proton mass difference (dashed thin line). In contrast to the electron-degenerate conditions found in past supernova simulations that fail to explode, the expanding hot plasma under neutrino irradiation favors electron fractions that exceed 0.5 as discussed in section 2.

The lower part in Figure 1d shows the neutrino and antineutrino abundances with dashed and dash-dotted lines respectively. The variations are rather due to density changes than luminosity variations. The upper part of Figure 1d shows the electron fraction from the simulation (thick solid line) and the equilibrium value determined by Eq. (1) (dotted line). The dash-dotted line in Figure 1a shows the reaction time scale as a function of radius. The upper branch belongs to infall, the lower branch to the ejection. Outside a radius of 600 km the reaction time scale is much larger than the dynamical time scale; during the drift phase of our mass element in the heating region it assumes values around 50 ms. Thus, the low electron fraction during infall is mainly set by the progenitor model. Before the shock front is crossed by the mass trajectory, the equilibrium Y_e is also low because many neutrons are bound in nuclei and not available as targets for antineutrino absorption. After the shock transition, matter is dissociated and higher electron fractions are favored. At first sight, the equilibrium electron fraction appears higher than expected at the given electron degeneracy.

The reason are neutrino absorption rates that are by an order of magnitude larger than the neutrino emission rates at these moderate temperatures. The thin solid line shows the high electron fraction equilibrium as it would evolve if only neutrino absorption were considered. The emission reactions alone favor a much lower equilibrium Y_e (thin dashed line) because there are only few positrons to capture under degenerate conditions. With the following rise of the temperature, however, the emission reactions gain weight with respect to the absorption reactions and the equilibrium Y_e correspondingly adjusts to lower values in the time window between $t = 235 - 275$ ms. But as the electron degeneracy is lifted with further temperature increase and expansion, and the electron chemical potential dips below half the neutron to proton mass difference, the emission rates start as well to favour higher electron fractions (steep rise of the thin dashed line). The equilibrium Y_e starts to increase again. The descent at very late time is, as in the beginning, due to the reappearance of nuclei. The electron fraction in the simulation (thick solid line) can now easily be understood: At each time it evolves towards the equilibrium value for the combined reactions (dotted line) at the pace of the local reaction time scale. It freezes out when the mass element is ejected. Note that for an analytical estimate of the electron fraction in our application one would have to combine the approximations for neutrino absorption rates in Eq. (64) in Qian & Woosley (1996) with the approximation for neutrino emission rates in Eqs. (9-10) in Beloborodov (2003) and to consider the reaction time scale in order to find the correct freeze-out value in the Y_e evolution.

We find that all simulations that lead to an explosion by neutrino heating develop a proton-rich environment around the mass cut with $Y_e > 0.5$. This is illustrated by the electron fraction profiles shown in Figure 1. The open circles denote the electron fraction of the run A40 at temperatures $T < 0.1 \times 10^9$ K for which we present nucleosynthesis details. The mass scale is normalized to the respective mass cut. The different runs from series A show an almost identical electron fraction profile at the mass cut. The competition by the reaction and ejection time scale is not directly influenced by the different explosion parameters, i.e. the enhanced neutrino diffusion at higher densities. The electron fraction profiles of series B, however, respond to the different reaction time scales set by the explosion parameters in the heating region. The electron fractions around and outside of $m_{\text{cut}} + 0.1 M_{\odot}$ are still close to the progenitor values. Differences in this region stem from the different locations of the mass cuts within the progenitor composition. It is important to note that the investigated region at the mass cut is highly unstable against convection because of a large negative entropy gradient. It is likely that the discrepancies in Y_e are heavily mixed on a dynamical time scale (Kifonidis et al. 2003). We expect, however, that the Y_e remains high in an averaged sense (see also Pruet et al. 2004). Moreover, matter blobs that leave the heating region in a environment of large convective turnover may still show qualitatively

similar features in comparison with our spherically symmetric shells because the high electron fraction in the neutrino field is enabled by the discussed general features of expanding hot matter. We believe that the dependence on the details of our different simulations is small.

5. Nucleosynthesis

For the nucleosynthesis results presented here, we consider only the first few zones outside of the mass cut enclosing a few hundredths of a solar mass where values of Y_e higher than 0.5 are achieved. An example for the influence of the individual weak interaction contributions leading to this change in Y_e is given in Figure 2 for an exploratory study of one mass zone.

The position of the mass cut emerges consistently from the simulation as the region of bifurcation in which the density has dropped below $\sim 10^6 \text{g/cm}^3$. Based on the temperature-density profiles of all the matter in our hydrodynamical simulation, the detailed nucleosynthesis is calculated in a postprocessing framework. The extended nuclear reaction network used consists of a fixed number of nuclei with $1 \leq Z \leq 50$, for details see Table 2. Neutral and charged particle reactions are taken from the recent REACLIB compilation (Rauscher & Thielemann 2000). For the weak interaction rates (electron/positron capture and beta decay) the rates by Fuller et al. (1982b,a) are used for nuclei with $A \leq 45$. In the mass range $45 < A \leq 65$ the extended tabulation by Langanke & Martínez-Pinedo (2001) is used. In Table 3 a detailed list of nuclei is given for which the above weak rates were utilized. The rates for neutrino and anti-neutrino captures on nuclei for the whole range of nuclei in the network are taken from a recent calculation (Zinner & Langanke 2004), based on the random phase approximation calculation of Langanke & Kolbe (2001, 2002). A complete list of nuclei for which neutrino and anti-neutrino capture reaction rates were included is shown in Table 4. Hence, all weak interactions responsible for changes of Y_e are taken into account in the reaction network, namely: neutrino/anti-neutrino capture on free neutrons and protons, neutrino/anti-neutrino capture on nuclei, electron/positron capture, and β^-/β^+ decays. Neutrino scattering processes are not included in the reaction network used for postprocessing as they do not contribute to changes of Y_e . Nevertheless, neutrino-induced spallation reactions can change the final abundances of some nuclei and we will investigate this in future calculations.

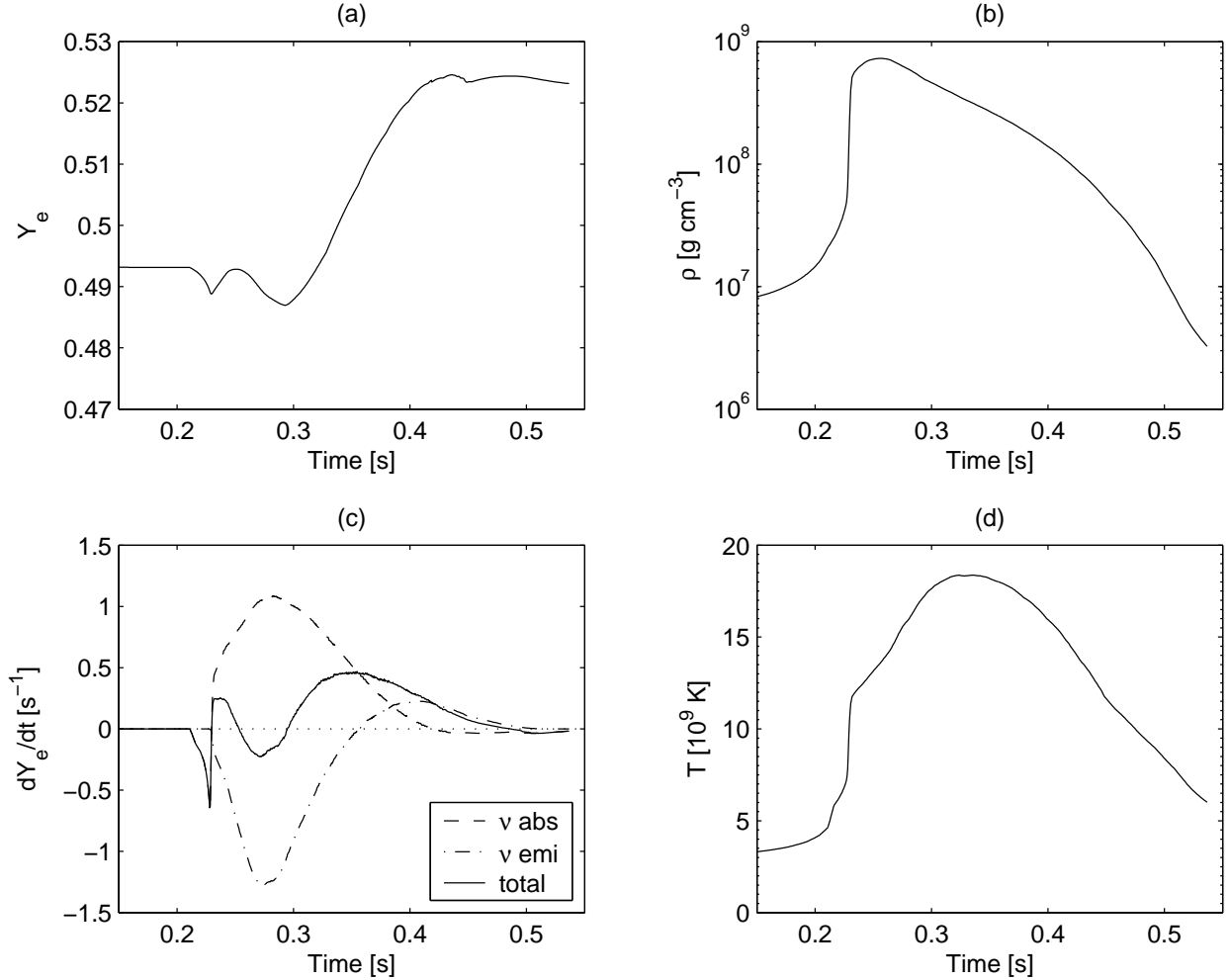


Fig. 2.— Hydrodynamical simulations with varied (reduced) neutrino scattering opacities (scattering cross sections on nucleons reduced by 40%) lead to larger neutrino luminosities and make successful supernova explosions possible. Here, we see the time evolution after core bounce of an ejected layer at $0.005M_{\odot}$ outside of the mass cut from a $20M_{\odot}$ supernova progenitor. Y_e indicates the neutron-richness of the ejected matter. (c) Contributions to the time derivative dY_e/dt due to neutrino absorptions and neutrino emissions on free nucleons. The quantities $\rho(t)$ and $T(t)$ indicate density and temperature. Note that Y_e depends strongly on both neutrino absorption and emission reactions and that in this exploding model Y_e in the innermost zones is larger than 0.5, i.e. proton-rich.

Table 2: List of nuclei in reaction network

Element	Mass Range	Element	Mass Range	Element	Mass Range
n	1	H	1–3	He	3–6
Li	6–9	Be	7–12	B	8–14
C	9–18	N	11–21	O	13–22
F	14–26	Ne	15–34	Na	17–40
Mg	19–38	Al	21–40	Si	22–42
P	23–48	S	24–50	Cl	26–42
Ar	27–44	K	29–48	Ca	30–50
SC	32–52	Ti	34–54	V	36–56
Cr	38–58	Mn	40–62	Fe	42–64
Co	44–66	Ni	46–68	Cu	48–70
Zn	51–74	Ga	53–86	Ge	55–78
As	57–80	Se	59–84	Br	61–86
Kr	64–92	Rb	66–92	Sr	68–94
Y	70–96	Zr	72–98	Nb	74–100
Mo	77–102	Tc	79–104	Ru	81–108
RH	83–110	Pd	86–114	Ag	88–116
Cd	90–118	In	92–120	Sn	94–126

Note. — Nuclear species used in nuclear reaction network for postprocessing. The mass range given indicates for each element the nuclei with the minimal and maximal neutron number.

Table 3: Nuclei for which electron and positron captures are included

Mass Number	Nuclides
1	n, H
21	Mg, Na, Ne, F, O
22	Mg, Na, Ne, F
23	Al, Mg, Na, Ne, F
24	Si, Al, Mg, Na, Ne
25	Si, Al, Mg, Na, Ne
26	Si, Al, Mg, Na
27	P, Si, Al, Mg, Na
28	S, P, Si, Mg, Na
29	S, P, Si, Al, Mg, Na
30	S, P, Si, Al
31	Cl, S, P, Si, Al
32	Ar, Cl, S, P, Si
33	Ar, Cl, S, P, Si
34	Ar, Cl, S, P, Si
35	K, Ar, Cl, S, P
36	Ca, K, Ar, Cl, S
37	Ca, K, Ar, Cl, S
38	Ca, K, Ar, Cl, S
39	Ca, K, Ar, Cl
40	Ti, Sc, Ca, K, Ar, Cl
41	Ti, Sc, Ca, K, Ar, Cl
42	Ti, Sc, Ca, K, Ar
43	Ti, Sc, Ca, K, Ar, Cl
44	V, Ti, Sc, Ca, K, Ar
45	Cr, V, Ti, Sc, Ca, K
46	Cr, V, Ti, Sc, Ca, K
47	Cr, V, Ti, Sc, Ca, K
48	Cr, V, Ti, Sc, Ca, K
49	Fe, Mn, Cr, V, Ti, Sc, Ca, K
50	Mn, Cr, V, Ti, Sc, Ca
51	Mn, Cr, V, Ti, Sc, Ca
52	Fe, Mn, Cr, V, Ti, Sc
53	Co, Fe, Mn, Cr, V, Ti
54	Co, Fe, Mn, Cr, V, Ti
55	Ni, Co, Fe, Mn, Cr, V, Ti
56	Ni, Co, Fe, Mn, Cr, V, Ti, Sc
57	Zn, Cu, Ni, Co, Fe, Mn, Cr, V
58	Cu, Ni, Co, Fe, Mn, Cr, V, Ti
59	Cu, Ni, Co, Fe, Mn, Cr, V
60	Zn, Cu, Ni, Co, Fe, Mn, Cr, V, Ti
61	Zn, Cu, Ni, Co, Fe
62	Ga, Zn, Cu, Ni, Co, Fe
63	Ga, Zn, Cu, Ni, Co, Fe
64	Ge, Ga, Zn, Cu, Ni, Co, Fe
65	Ge, Ga, Zn, Cu, Ni, Co

Note. — All nuclei per given mass number for which weak interactions by Fuller et al. (1982b,a) and by Langanke & Martínez-Pinedo (2001) are used in the nuclear network.

Table 4: Nuclei for which neutrino and anti-neutrino captures are included

Element	Mass Range (ν capture)	Mass Range ($\bar{\nu}$ capture)
n	1	1
H	1	1
He	6	6
Li	7–9	7–9
Be	8–12	8–12
B	10–14	10–14
C	11–18	11–18
N	13–21	13–21
O	14–22	14–22
F	16–26	16–26
Ne	18–29	17–29
Na	20–32	19–22
Mg	21–35	21–35
Al	22–37	22–37
Si	24–39	23–39
P	26–42	25–42
S	28–42	27–42
Cl	30–42	29–42
Ar	32–44	31–44
K	34–48	33–48
Ca	36–50	35–50
Sc	38–52	37–52
Ti	40–54	39–54
V	42–56	41–56
Cr	44–58	43–58
Mn	45–62	45–62
Fe	48–64	46–64
Co	50–66	49–66
Ni	52–68	51–68
Cu	54–70	53–70
Zn	56–74	55–74
Ga	58–78	57–78
Ge	60–78	59–78
Se	67–84	66–84
Br	69–86	68–86
Kr	71–92	70–92
Rb	73–92	72–92
Sr	77–80	74–80

Note. — Nuclides for which neutrino and anti-neutrino capture reactions are included in the nuclear network. The mass range given indicates for each element the nucleus with the lowest mass number and the nucleus with the highest mass number.

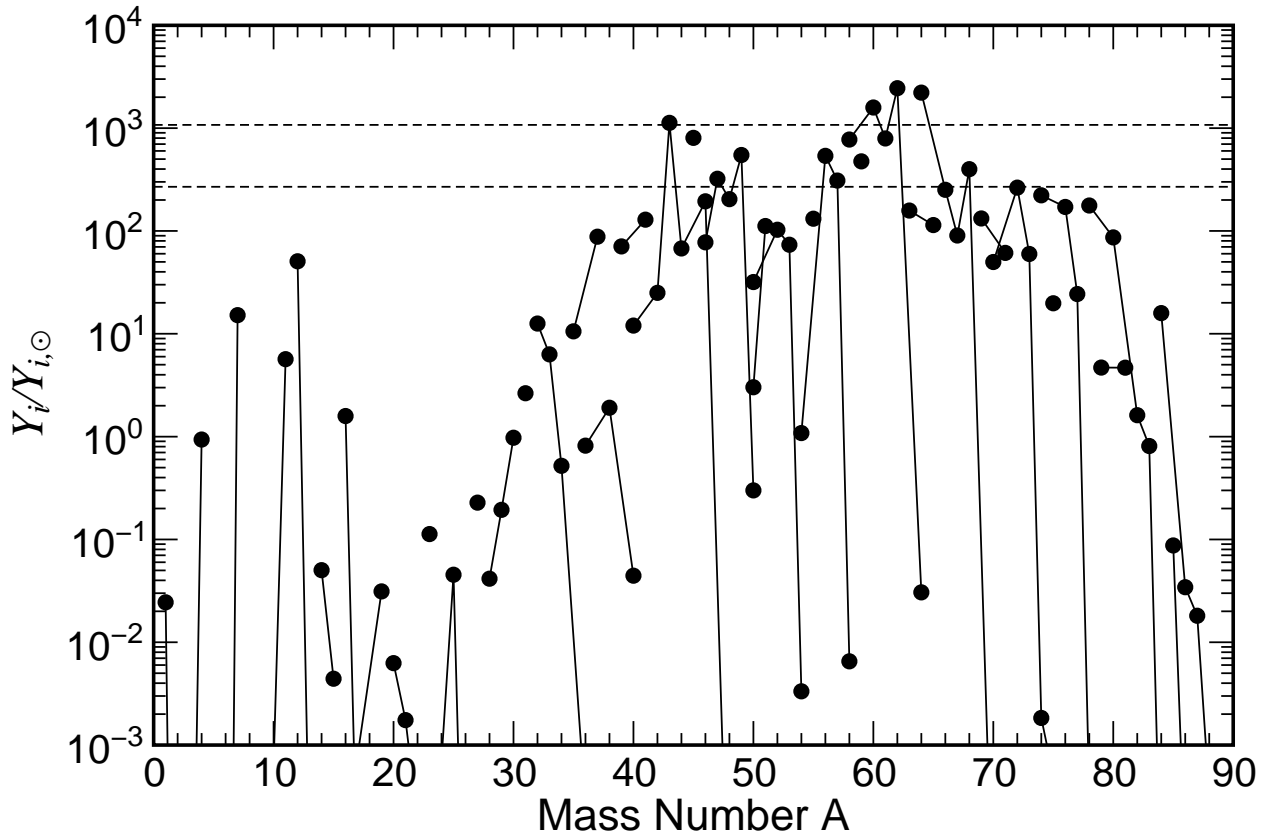


Fig. 3.— Abundances for model A40 relative to solar abundances.

Figure 3 shows the abundances after decay to stability of the different nuclei for model A40 integrated over mass zones with $Y_e > 0.5$, including in total $\sim 0.04 M_\odot$. In this model, the mass cut is located at $1.511 M_\odot$ and the explosion energy is 0.78×10^{51} erg. For these mass zones, we are only concerned with the Fe-group composition. In Figure 3 isotopic abundances relative to solar values are plotted, resulting from postprocessing based on the hydrodynamical profiles and employing the full nuclear reaction network including neutrino and anti-neutrino capture reactions. Neutrino induced reactions are important for the nucleosynthesis of nuclei in the mass range $A > 62$. These nuclei are mainly produced in the zones close to the mass cut where the electron fraction strongly depends on the neutrino captures. For these mass zones relatively high entropies are attained: $s/k_b \sim 20\text{--}47$ (See Figure 4). In nucleosynthesis terms this corresponds to complete explosive Si-burning with a strong alpha-rich freeze-out which even leaves a finite proton abundance ($0.0007 M_\odot$) due to Y_e being larger than 0.5. The high proton abundance permits the onset of an rp-process which, however, does not proceed too far in A as (due to the high entropies) the densities are too small. The abundances result from the accumulation of matter at the waiting-point nuclei ^{64}Ge , ^{68}Se , ^{72}Kr , ^{76}Sr . After decay to stability they produce the high abundances of

^{64}Zn , ^{68}Zn , ^{72}Ge , and ^{76}Se . A relatively high abundance of ^{78}Kr is also obtained. ^{78}Kr is considered to be produced by the p-process in the ONe layers of the star. Our proton-rich environment constitutes an alternative or complementary production site for these isotopes. Chemical evolution studies (e.g. Timmes et al. 1995) underproduce ^{64}Zn by about a factor 5. Umeda & Nomoto (2005) have found that the $^{64}\text{Zn}/^{56}\text{Fe}$ ratio is enhanced *if* Ye is close to 0.5 and the explosion energy is as high as $\sim 10^{52}$ erg. A possible site for the production of ^{64}Zn is the modest early-time neutrino-driven wind occurring after core bounce in supernovae (Woosley & Hoffman 1992). Our proton-rich ejecta would provide larger quantities than in the neutrino wind.

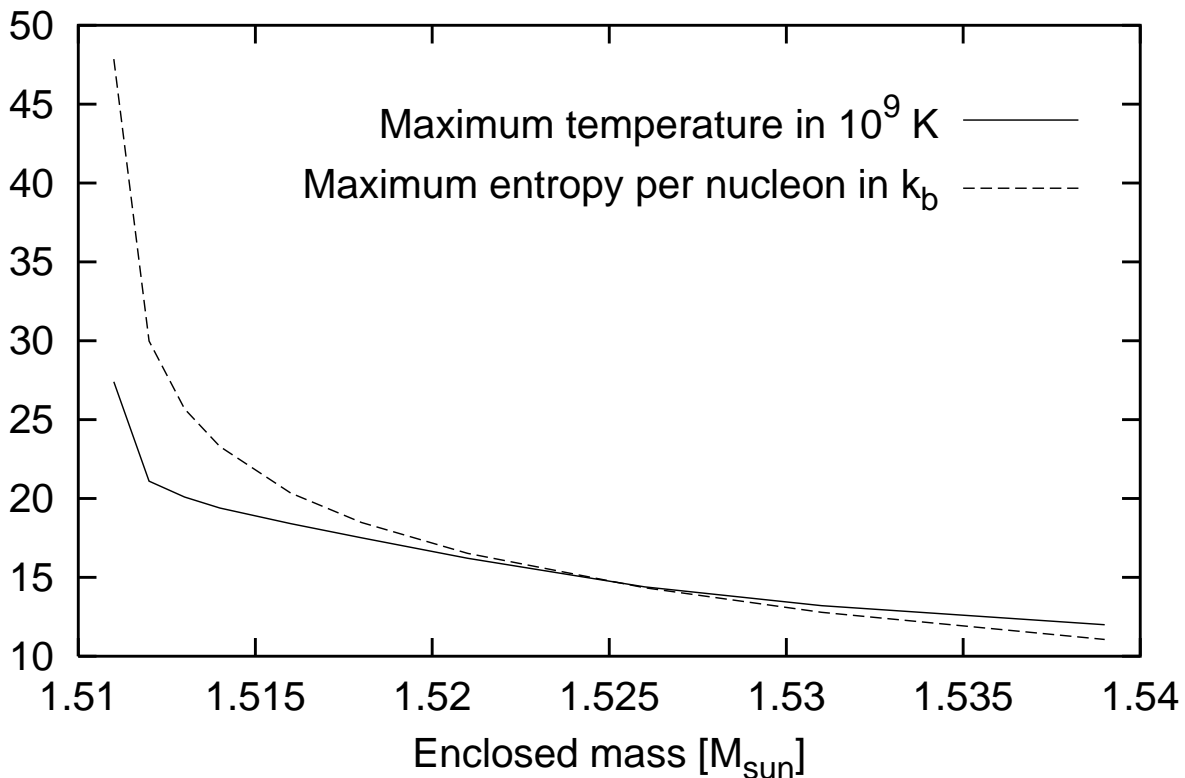


Fig. 4.— Maximum entropy and maximum temperature of each mass zone versus enclosed mass. The temperature is given in units of 10^9 K (solid line); the entropy is given per nucleon in units of the Boltzmann constant k_b (dashed line).

For the intermediate mass elements the main improvement compared to earlier calculations is the higher production of individual nuclei like ^{45}Sc and ^{49}Ti . Scandium is mainly produced by the β^+ -decays originating from ^{45}Cr and ^{45}V decaying via ^{45}Ti to ^{45}Sc . Different calculations of abundance yields (Thielemann et al. 1996; Woosley & Weaver 1995; Chieffi & Limongi 2002) fail to predict the observed abundance of scandium (Gratton & Sneden

1991; Cayrel et al. 2004). Our calculations show that Sc can be consistently produced with iron in the inner regions of the supernova where Y_e is higher than 0.5. The ejected yield of Sc is $10^{-6} M_\odot$ which is a factor of 10 larger than the value obtained for a similar star by Thielemann et al. (1996). If we assume that our total production of Fe is similar to the one obtained in the cited work our Sc yield will be consistent with observations. ^{49}Ti is underproduced by a factor 5 in the chemical evolution studies of Timmes et al. (1995). The nucleus ^{49}Ti originates from the decay chain of ^{49}Mn which decays via ^{49}Cr and ^{49}V to ^{49}Ti . After decay to stability, the resulting yield of ^{49}Ti is $3 \times 10^{-6} M_\odot$. We find that the origin of the differences in nucleosynthesis yields is a consequence of an electron fraction above 0.5 which is due to a consistent treatment of all weak interaction processes on free nucleons. The obtained Y_e values are not sensitive to the inclusion of neutrino and anti-neutrino captures on nuclei. However, neutrino and anti-neutrino capture reactions on nuclei decrease the abundances of nuclei like ^{16}O , ^{20}Ne , $^{56,57}\text{Co}$ and increase the abundances of ^{32}S , ^{36}Ar , $^{53,54}\text{Fe}$, ^{55}Co , ^{59}Ni , ^{59}Cu . All of the above nuclei have changes in abundances of more than 20% due to the inclusion of neutrino/anti-neutrino captures on nuclei. This effect is only important for the nucleosynthesis yields of the Fe-group as the main origin of ^{16}O , ^{20}Ne , ^{32}S , ^{36}Ar is located in different regions of the supernova.

In the absence of a (yet) complete nucleosynthesis calculation for the whole Fe-group production we combine our abundances with the results of Thielemann et al. (1996). The two calculations are combined in such a way that the resulting amount of Fe-group elements is the same as in this earlier work. For the inner zones where neutrino and anti-neutrino capture reactions play an important role the results of the present calculation are used. They constitute about 30% of the total production of Fe-group elements. For the other zones where neutrino/anti-neutrino captures have no significant influence for the final Y_e we use the abundance results from the above cited work. This procedure allows us to estimate the influence of a consistent treatment of weak interaction processes on the total production of Fe-group elements. To further solidify these results full nucleosynthesis calculations will be performed based on the exploding models.

In a recent work, Pruet et al. (2004) have studied a similar scenario (with a similar philosophy) for the innermost ejected layers, based on a 2D simulation by Janka et al. (2003). While the original 2D simulation did not yield an explosion, omitting the velocity-dependent terms from the neutrino momentum equation resulted in a successful explosion. Their nucleosynthesis results are based on calculations for tracer particles. They find results in agreement with our results. However, they do not report on the production of heavy nuclei with $A > 64$.

Figure 6 shows elemental abundances of two calculations compared to two sets of ob-

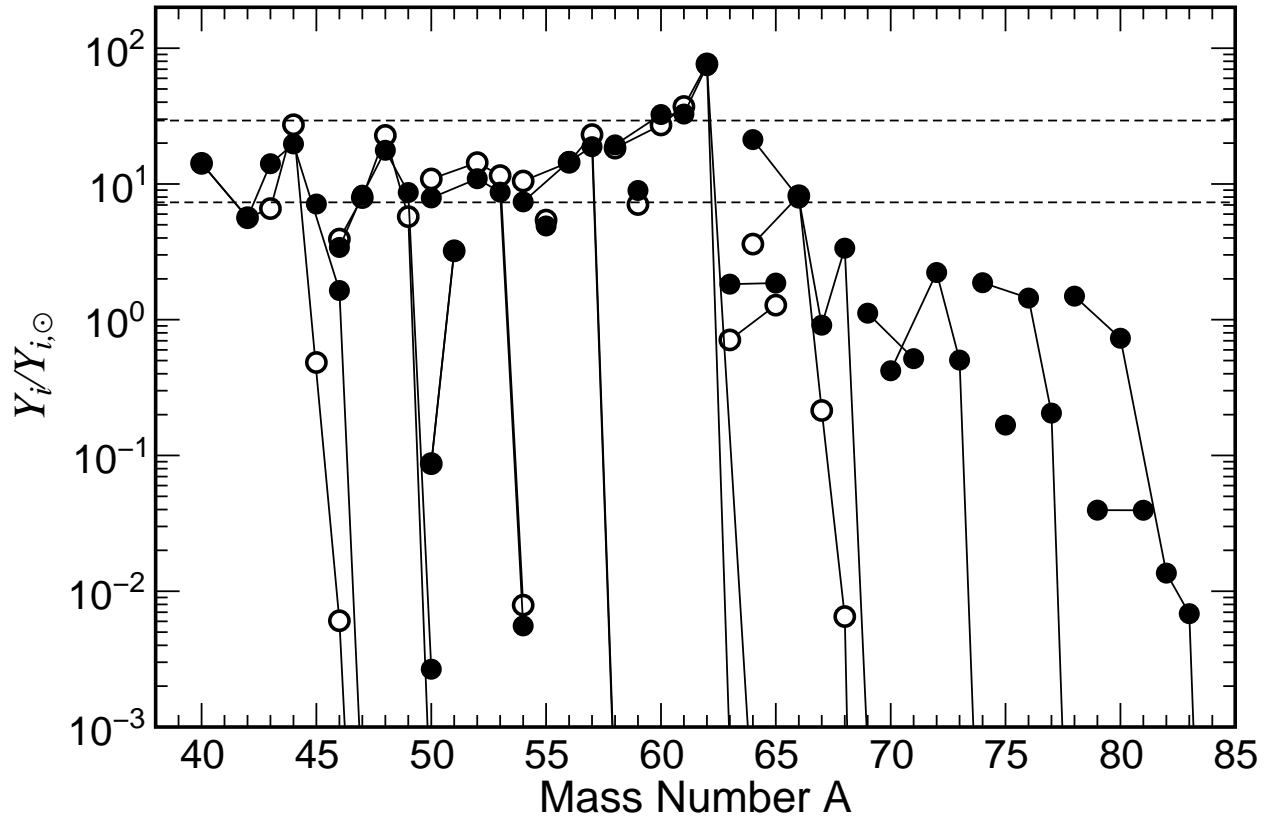


Fig. 5.— Combined abundances of this work (model A40) and Thielemann et al. (1996). The filled circles are the combined abundances and the open circles are the original abundances of the above reference. For details see text.

servational data. One set of observational data (Gratton & Sneden 1991) originates from a sample of stars with $-2.7 < [\text{Fe}/\text{H}] < -1$, relevant for the average type II supernova contribution. The second set of observational data represents a sample of extremely metal-poor stars (Cayrel et al. 2004). The nucleosynthesis results of this work are shown in combination with the results of the earlier calculation as shown in Figure 5. For comparison the theoretical prediction by Thielemann et al. (1996) is also shown. We see clearly an improvement for Sc and the heavy elements Cu and Zn. Vanadium is not yet explained but might also require future observational investigations.

6. Conclusions

Presently self-consistent core collapse supernova simulations in 1D and 2D do not lead to successful explosions. Remaining uncertainties in neutrino opacities and/or the expected strong influence of convection (due to hydrodynamic instabilities caused by entropy gradients and/or rotation and magnetic fields) are likely to change this result. They lead either to higher neutrino luminosities or higher efficiencies of neutrino energy deposition via neutrino and anti-neutrino captures on nucleons. In order to test the accompanied nucleosynthesis aspects in 1D calculations of successful explosions, we performed simulations with variations in neutrino scattering cross sections on nucleons and/or neutrino and anti-neutrino captures on neutrons and protons. In both cases successful explosions emerge with an interesting evolution of the Y_e gradient in the innermost ejecta, which were followed up by a postprocessing of such layers for nucleosynthesis purposes.

The detailed nucleosynthesis calculations with a consistent treatment of all weak interactions show an electron fraction $Y_e > 0.5$, i.e. a slightly proton-rich environment with relatively high entropies of up to $\sim 50 k_B$ per nucleon. This causes complete Si-burning with an alpha-rich (and proton-rich) freeze-out. About $0.0007 M_\odot$ of hydrogen remain in the innermost ejecta without a need to mix this matter in from the hydrogen envelope. Such a proton-rich environment at relatively high entropies permits a combination of an rp-process and a p-process which produces also nuclei beyond $A=62$, up to $A=80$, with a major contribution to ^{64}Zn . The rp-process does not extend to higher masses as the high entropies imply too small densities for a path at very small proton separation energies.

In addition, we find improvements within the Fe-group. The strong overabundances of $^{58,62}\text{Ni}$ found in previous (too neutron-rich) environments are reduced. ^{45}Sc and ^{49}Ti are enhanced to permit predictions closer to solar proportions. Especially the emergence of ^{45}Sc seems to be a solution to the previously not understood abundance of this only stable isotope of Sc. This discussion is also interesting with respect to ^{44}Ti , made in the alpha-rich freeze-

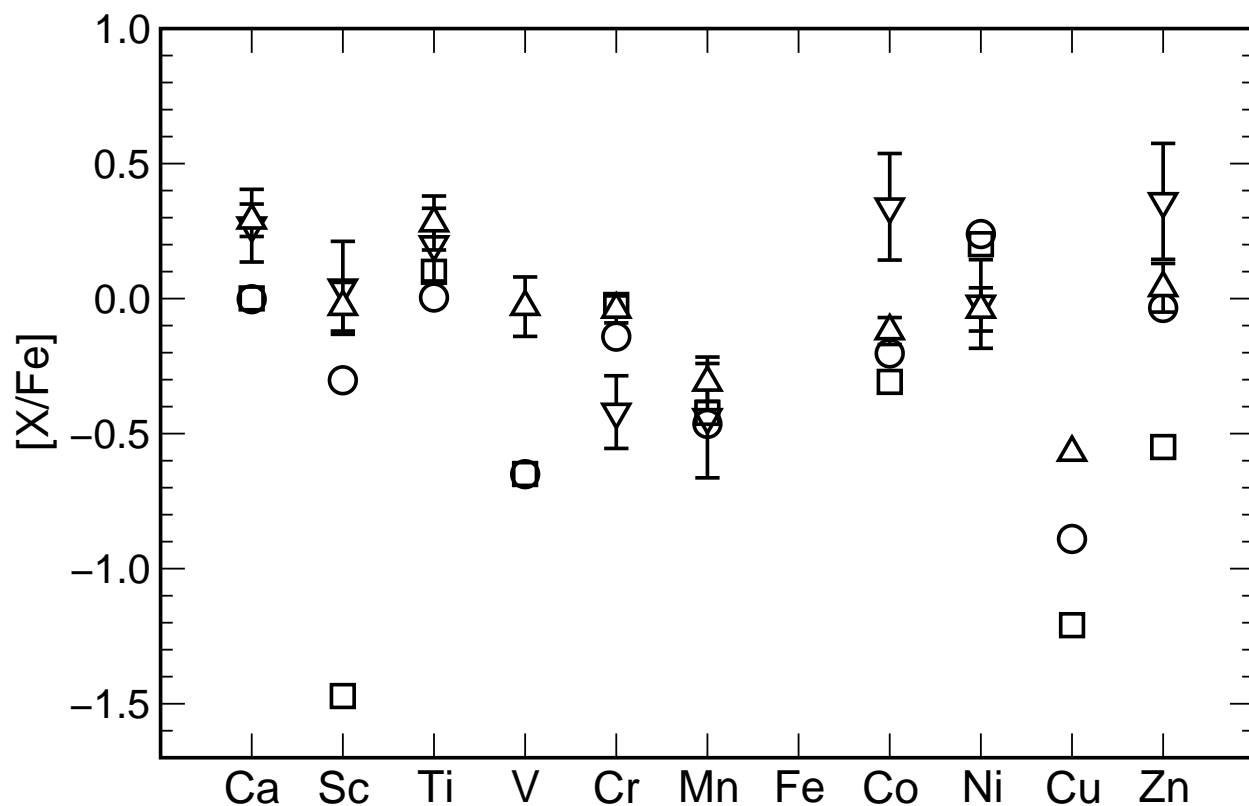


Fig. 6.— Comparison of elemental overabundance in the mass range Ca to Zn for different calculations. The triangles with error bars represent observational data. The triangles facing upwards (Gratton & Sneden 1991) originate from an analysis of stars with $-2.7 < [\text{Fe}/\text{H}] < -0.2$. The triangles facing downwards (Cayrel et al. 2004) is data for a sample of extremely metal poor stars ($-4.1 < [\text{Fe}/\text{H}] < -2.7$). The circles are abundances of this work combined with the work of Thielemann et al. (1996) to obtain the same amount of Fe-group elements. The squares show the pure abundances of the previous reference.

out in the inner explosive ejecta. ^{44}Ti is sensitive to Y_e and reduced in the mass range where ^{45}Sc is high. This will influence the overall predictions of ^{44}Ti .

Values of $Y_e > 0.5$ are due to the neutrino interactions with matter under electron non-degenerate conditions in a convectively unstable domain and thus related to the explosion mechanism. The effect of neutrinos decreases with $1/r^2$ and about 50-60% of the Fe-group ejecta (the outer part of explosive, complete Si-burning) is determined by values of Y_e equal to or close to the initial values inherited from stellar evolution. In this first study we have tried to give an estimate for the overall Fe-group composition based on such a superposition of the present results for the innermost ejecta with those of (Thielemann et al. 1996). Future investigations will require to perform full nucleosynthesis calculation for complete stars based on these exploding models. They will also require a sensitivity test of the nucleosynthesis results to the scaling factors for neutrino-induced reactions discussed in Figure 1 and in combination with the position of the mass cut and the explosion energy. This should be considered in order to reproduce results for supernovae where detailed observational information in abundances, gamma-ray emitters and explosion energies is available.

This work is partly supported by the Swiss NSF grant 2000-061031.02 and by the Spanish MCyT and European Union ERDF under contracts AYA2002-04094-C03-02 and AYA2003-06128. The neutrino transport calculations have been performed on the CITA Itanium I. A.M. is supported at the Oak Ridge National Laboratory, which is managed by UT-Battelle, LLC for the DOE under contract DE-AC05-00OR22725. He is also supported in part by a DOE ONP Scientific Discovery through Advanced Computing Program grant.

REFERENCES

- Argast, D., Samland, M., Thielemann, F.-K., & Gerhard, O. E. 2002, *A&A*, 388, 842
- Argast, D., Samland, M., Thielemann, F.-K., & Qian, Y.-Z. 2004, *A&A*, 416, 997
- Arnett, W. D. & Schramm, D. N. 1973, *ApJ*, 184, L47
- Aufderheide, M. B., Baron, E., & Thielemann, F.-K. 1991, *ApJ*, 370, 630
- Baade, W. & Zwicky, F. 1934, *Proceedings of the National Academy of Science*, 20, 259
- Baron, E., Bethe, H. A., Brown, G. E., Cooperstein, J., & Kahana, S. 1987, *Phys. Rev. Lett.*, 59, 736
- Baron, E., Cooperstein, J., & Kahana, S. 1985, *Phys. Rev. Lett.*, 55, 126
- Beloborodov, A. M. 2003, *ApJ*, 588, 931
- Bethe, H. A. 1990, *Rev. Mod. Phys.*, 62, 801
- Bethe, H. A. & Wilson, J. R. 1985, *ApJ*, 295, 14
- Bravo, E., Dominguez, I., Isern, J., Canal, R., Hoefflich, P., & Labay, J. 1993, *A&A*, 269, 187
- Bruenn, S. W. 1985, *ApJS*, 58, 771
- Bruenn, S. W. 1989, *ApJ*, 340, 955
- Bruenn, S. W., Raley, E. A., & Mezzacappa, A. 2004, astro-ph/0404099
- Buras, R., Rampp, M., Janka, H.-T., & Kifonidis, K. 2003, *Phys. Rev. Lett.*, 90, 241101
- Burrows, A. 1990, *Ann. Rev. Nucl. Part. Sci.*, 40, 181
- Burrows, A., Hayes, J., & Fryxell, B. A. 1995, *ApJ*, 450, 830
- Burrows, A., Reddy, S., & Thompson, T. A. 2004, *Nucl. Phys. A*, in press
- Cayrel, R., Depagne, E., Spite, M., Hill, V., Spite, F., François, P., Plez, B., Beers, T., Primas, F., Andersen, J., Barbuy, B., Bonifacio, P., Molaro, P., & Nordström, B. 2004, *A&A*, 416, 1117
- Chieffi, A. & Limongi, M. 2002, *ApJ*, 577, 281

- Colgate, S. A. & White, R. H. 1966, *ApJ*, 143, 626
- Fröhlich, C., Hauser, P., Liebendörfer, M., Martínez-Pinedo, G., Bravo, E., Hix, W. R., Zinner, N. T., & Thielemann, F.-K. 2004, *Nucl. Phys. A*, in press, (astro-ph/0408067)
- Fryer, C. L. & Warren, M. S. 2004, *ApJ*, 601, 391
- Fuller, G. M., Fowler, W. A., & Newman, M. J. 1982a, *ApJ*, 252, 715
- . 1982b, *ApJS*, 48, 279
- Gratton, R. G. & Sneden, C. 1991, *A&A*, 241, 501
- Herant, M., Benz, W., Hix, W. R., Fryer, C. L., & Colgate, S. A. 1994, *ApJ*, 435, 339
- Hix, W. R., Messer, O. E. B., Mezzacappa, A., Liebendörfer, M., Sampaio, J., Langanke, K., Dean, D. J., & Martínez-Pinedo, G. 2003, *Phys. Rev. Lett.*, 91
- Honda, S., Aoki, W., Ando, H., Izumiura, H., Kajino, T., Kambe, E., Kawanomoto, S., Noguchi, K., Okita, K., Sadakane, K., Sato, B., Takada-Hidai, M., Takeda, Y., Watanabe, E., Beers, T. C., Norris, J. E., & Ryan, S. G. 2004, *ApJS*, 152, 113
- Horowitz, C. J. 2002, *Phys. Rev. D*, 65
- Janka, H.-T., Buras, R., & Rampp, M. 2003, *Nucl. Phys. A*, 718, 269
- Janka, H.-T. & Müller, E. 1996, *A&A*, 306, 167
- Keil, W., Janka, H.-T., & Müller, E. 1996, *ApJ*, 473, L111+
- Kifonidis, K., Plewa, T., Janka, H.-T., & Müller, E. 2003, *A&A*, 408, 621
- Koshiha, M. 1992, *Phys. Rep.*, 220, 229
- Langanke, K. & Kolbe, E. 2001, *At. Data Nucl. Data Tables*, 79, 293
- . 2002, *At. Data Nucl. Data Tables*, 82, 191
- Langanke, K. & Martínez-Pinedo, G. 2001, *At. Data Nucl. Data Tables*, 79, 1
- Langanke, K., Martínez-Pinedo, G., Messer, O. E. B., Sampaio, J. M., Dean, D. J., Hix, W. R., Mezzacappa, A., Liebendörfer, M., Janka, H.-T., & Rampp, M. 2003, *Phys. Rev. Lett.*, 90
- Liebendörfer, M., Messer, O. E. B., Mezzacappa, A., Bruenn, S. W., Cardall, C. Y., & Thielemann, F.-K. 2004, *ApJS*, 150, 263

- Liebendörfer, M., Mezzacappa, A., & Thielemann, F.-K. 2001, *Phys. Rev. D*, 63, 104003
- Liebendörfer, M., Rosswog, S., & Thielemann, F.-K. 2002, *ApJS*, 141, 229
- Liebendörfer, M., Mezzacappa, A., Thielemann, F.-K., Messer, O. E. B., Hix, W. R., & Bruenn, S. W. 2001, *Phys. Rev. D*, 63, 103004
- Mayle, R. & Wilson, J. R. 1988, *ApJ*, 334, 909
- Messer, O. E. B., Mezzacappa, A., Bruenn, S. W., & Guidry, M. W. 1998, *ApJ*, 507, 353
- Mezzacappa, A. & Bruenn, S. W. 1993a, *ApJ*, 405, 637
- . 1993b, *ApJ*, 410, 740
- Mezzacappa, A., Calder, A. C., Bruenn, S. W., Blondin, J. M., Guidry, M. W., Strayer, M. R., & Umar, A. S. 1998, *ApJ*, 495, 911
- Mezzacappa, A., Liebendörfer, M., Messer, O. E. B., Hix, W. R., Thielemann, F.-K., & Bruenn, S. W. 2001, *Phys. Rev. Lett.*, 86, 1935
- Mezzacappa, A. & Messer, O. E. B. 1999, *Journal of Computational and Applied Mathematics*, 109, 281
- Myra, E. S. & Bludman, S. A. 1989, *ApJ*, 340, 384
- Nakamura, T., Umeda, H., Iwamoto, K., Nomoto, K., Hashimoto, M., Hix, W. R., & Thielemann, F. 2001, *ApJ*, 555, 880
- Nakamura, T., Umeda, H., Nomoto, K., Thielemann, F., & Burrows, A. 1999, *ApJ*, 517, 193
- Nomoto, K. & Hashimoto, M. 1988, *Phys. Rep.*, 163, 13
- Nomoto, K., Hashimoto, M., Tsujimoto, T., Thielemann, F.-K., Kishimoto, N., Kubo, Y., & Nakasato, N. 1997, *Nucl. Phys. A*, 616, 79
- Oppenheimer, J. R. & Snyder, H. 1939, *Phys. Rev.*, 455
- Pruet, J., Woosley, S. E., Buras, R., Janka, H.-T., & Hoffman, R. D. 2004, *astro-ph/0409446*
- Qian, Y. Z., Haxton, W. C., Langanke, K., & Vogel, P. 1997, *Phys. Rev. C*, 55, 1532
- Qian, Y.-Z. & Woosley, S. E. 1996, *ApJ*, 471, 331
- Rampp, M. & Janka, H.-T. 2000, *ApJ*, 539, L33

- Rauscher, T., Heger, A., Hoffman, R. D., & Woosley, S. E. 2002, *ApJ*, 576, 323
- Rauscher, T. & Thielemann, F.-K. 2000, *At. Data Nucl. Data Tables*, 75, 1
- Snedden, C., Cowan, J. J., Lawler, J. E., Ivans, I. I., Burles, S., Beers, T. C., Primas, F., Hill, V., Truran, J. W., Fuller, G. M., Pfeiffer, B., & Kratz, K. 2003, *ApJ*, 591, 936
- Takahashi, K., Witt, J., & Janka, H.-T. 1994, *A&A*, 286, 857
- Terasawa, M., Sumiyoshi, K., Yamada, S., Suzuki, H., & Kajino, T. 2002, *ApJ*, 578, L137
- Thielemann, F.-K., Hashimoto, M., & Nomoto, K. 1990, *ApJ*, 349, 222
- Thielemann, F.-K., Nomoto, K., & Hashimoto, M. 1996, *ApJ*, 460, 408
- Thompson, C. 2000, *ApJ*, 534, 915
- Thompson, T. A., Burrows, A., & Meyer, B. S. 2001, *ApJ*, 562, 887
- Thompson, T. A., Burrows, A., & Pinto, P. A. 2003, *ApJ*, 592, 434
- Thompson, T. A., Quataert, E., & Burrows, A. 2004, *astro-ph/0403224*
- Timmes, F. X., Woosley, S. E., & Weaver, T. A. 1995, *ApJS*, 98, 617
- Umeda, H. & Nomoto, K. 2002, *ApJ*, 565, 385
- . 2005, *ApJ*, 618, in press
- Wanajo, S., Kajino, T., Mathews, G. J., & Otsuki, K. 2001, *ApJ*, 554, 578
- Wilson, J. R. & Mayle, R. W. 1993, *Phys. Rep.*, 227, 97
- Woosley, S. E. & Hoffman, R. D. 1992, *ApJ*, 395, 202
- Woosley, S. E. & Weaver, T. A. 1986, *ARA&A*, 24, 205
- Woosley, S. E. & Weaver, T. A. 1995, *ApJS*, 101, 181
- Woosley, S. E., Wilson, J. R., Mathews, G. J., Hoffman, R. D., & Meyer, B. S. 1994, *ApJ*, 433, 229
- Zinner, T. N. & Langanke, K. 2004, private communication